scientific reports

Check for updates

OPEN

Functional ultrasound and brain connectivity reveal central nervous system compromise in Trembler-J mice model of Charcot-Marie-Tooth disease

Maximiliano Anzibar Fialho[1,2], Mariana Martínez Barreiro[3], Lucia Vázquez Alberdi[3], Juan Pablo Damián[4,5], Maria Vittoria Di Tomaso[6], Jérôme Baranger[7], Mickael Tanter[7], Miguel Calero[8], Carlos Negreira[1], Nicolás Rubido[9], Alejandra Kun[3,10,11]✉ & Javier Brum[1,11]✉

The Charcot-Marie-Tooth-1E (CMT1E) disease is typically described as a peripheral neuropathy in humans, causing decreased nerve conduction, spastic paralysis, and tremor. The Trembler-J (TrJ) mice serve as a high fidelity model of this disease. Here, we use functional ultrasound (fUS) and functional connectivity (FC) to analyze TrJ mice's brain activity during sensory stimulation and resting state experiments against wild type (WT) mice - the healthy counterpart. fUS is an imaging technique that measures cerebral blood volume (CBV) temporal changes. We study these changes in the primary somatosensory cortex barrel field (S1BF) of both mice populations during periodic vibrissae stimulation, measuring the number of pixels that correlate to the stimulation (i.e., the size of the activation area), the average correlation of these pixels (i.e., the response strength), and the CBV's rate of change for each stimulation (i.e., the hemodynamic response). Then, we construct a FC matrix for each genotype and experiment by correlating the CBV signals from the eight cortical regions defined by the Paxinos and Franklin atlas. Our results show that TrJ mice have significantly diminished neurovascular responses and altered brain connectivity with respect to WT mice, pointing to central nervous system effects that could shift our understanding of the CMT1E disease.

The Charcot-Marie-Tooth's disease (CMT) groups the most frequent hereditary, chronic, progressive, sensory-motor peripheral neuropathies. CMT is caused by mutations in over 100 genes[1–3]. In particular, mutations on the *pmp22* (gene), coding Schwann cell myelin protein PMP22, cause 70% of myelinopathies (CMT1)[4–6]. The human subtype CMT1E share with Trembler-J (TrJ) mice the same *pmp22* spontaneous point mutation (T1703C) in the homologous murine gene[7–9], preventing its myelin insertion, and generating intracellular PMP22 aggregates[10,11]. The main clinical manifestations include decreased nerve conduction velocity, spastic paralysis, and generalized tremor. These manifestations are comparable in humans and TrJ mice[12–17].

There is some evidence that *pmp22* may play roles other than peripheral nerve myelination. Our group detected the PMP22 protein in Schwann cells' nuclei of TrJ and wild type (WT) mice associated with regions of transcriptionally active chromatin, suggesting a possible nuclear role of PMP22 which is not well established[18].

[1]Laboratorio deAcústica Ultrasonora, Instituto de Física, Facultad de Ciencias, Universidad de la República, 11400 Montevideo, Uruguay. [2]Física No Lineal, Instituto de Física de Facultad de Ciencias, Universidad de la República, 11400 Montevideo, Uruguay. [3]Laboratorio de Biología Celular del Sistema Nervioso Periférico, Departamento de Proteínas y ÁcidosNucleicos, Instituto de Investigaciones Biológicas Clemente Estable, 11600 Montevideo, Uruguay. [4]Departamento de Biociencias Veterinarias, Facultad de Veterinaria, Universidad de la República, 13000 Montevideo, Uruguay. [5]Núcleo de Bienestar Animal, Facultad de Veterinaria, Universidad de la República, 13000 Montevideo, Uruguay. [6]Departamento de Genética, Instituto de Investigaciones Biológicas Clemente Estable, 11600 Montevideo, Uruguay. [7]Institute Physics for Medicine Paris, Inserm U1273, ESPCI Paris, CNRS UMR 8063, PSL University, 75015 Paris, France. [8]Chronic Disease Programme (UFIEC), and CIBERNED, Instituto de Salud Carlos III, 28220 Majadahonda, Madrid, Spain. [9]Institute for Complex Systems and Mathematical Biology, University of Aberdeen, King's College, AB24 3UE Aberdeen, UK. [10]Sección Bioquímica, Facultad de Ciencias, Universidad de la República, 11400 Montevideo, Uruguay. [11]Alejandra Kun and Javier Brum have contributed equally to this work. ✉email: akun@fcien.edu.uy; javier.brum@fcien.edu.uy

Moreover, we have been the first to report the hippocampal expression of PMP22. We demonstrated a differential expression of the PMP22 protein in the CA3 region of TrJ compared to the WT counterpart, which we associated with an anxious phenotype of TrJ[19]. This body of evidence could have systemic-level consequences for brain activity.

Over the last decade, functional ultrasound (fUS) has proven to be a powerful tool to examine brain activity by measuring the changes in cerebral blood volume (CBV)[20–27]. CBV is quantified from Doppler imaging with respect to the number of red blood cells in a given brain volume. The neural activity in the brain and the CBV changes are related through the neurovascular coupling. This is a regulated mechanism of the functional neurovascular complex operating in the functional neurovascular unit (composed of neurons, astrocytes, microglia, pericytes and endothelial cells). This mechanism allows to locally adapt the cerebral blood flow according to the neuronal activity, ensuring the necessary supply of oxygen and nutrients at all times[28].

Thus, the hemodynamic measurements obtained using fUS are a reliable representation of the electrophysiological activity associated with neurons. This has been corroborated, for example, by Sieu et al.[29], who described this relationship during wakefulness in mobile rats, and Bourgeais-Rambur et al.[30], who combined fUS with local field potentials to study the spread of depolarization associated with migraine. Similarly, Nunez-Elizalde et al.[31] also showed that blood flow fluctuations are directly correlated with neural activity, comparing fUS measurements with high spatial resolution electrophysiology. Moreover, the relationship between CBV changes and calcium activity of neurons has also been studied using high spatial resolution techniques, such as confocal microscopy[32]. As such, fUS has been successfully used to map the activity of specific brain regions during different cognitive states[24] in rodents[22], primates[23], and humans[25,26].

A common approach to understand brain dynamics under different settings is to study its functional connectivity (FC), i.e., the functional links emerging between anatomically different regions (possibly without axonal projections) due to similar electrophysiological activity or hemodynamic responses. In this sense, fUS has revealed FC patterns during resting state (i.e., task free), firstly in rats[33], and then in primates[24], mice[34] and human neonates[27]. These FC patterns are consistent with those found with functional magnetic resonance imaging (which is another way to indirectly measure brain activity)[35]. Overall, analyzing FC is an excellent way to quantify changes due to behaviour, tasks, and importantly, due to acute or chronic neuropathologies[36]. For example, Rahal et al.[37] found alterations in brain connectivity of fUS data due to sustained inflammatory pain or arthritis, and Rabut et al.[38] mapped the FC to the time/dose response of scopolamine (a psychoactive drug), which led other researchers[39] to improve the understanding of how drugs affect brain functionality and the development of pharmacological treatments for several neurological diseases. Consequently, fUS can be used along FC analyses to improve our understanding of different neuropathies, including the study of CMT1E in TrJ and the unknown physiological mechanisms associated with the central expression of the disease.

In this work, we use fUS measurements and functional connectivity analysis to study the central nervous system responses to specific external stimuli in WT and TrJ mice - the murine model of human CMT1E. Specifically, we analyze the vibrissae sensory path by measuring the activation area in the somatosensory cortex, as well as the strength of the correlation with stimuli and the CBV rate of change during stimulation. Moreover, we study the brain connectivity under stimulation and resting states in both genotypes. We generate connectivity matrices for eight anatomic regions including the cortex and the hippocampus. Our results show that TrJ mice present an altered central nervous response in comparison with WT, indicating a compromise of the neurovascular system due to the disease. The present work complements our previous observations around the hippocampal domains, where we showed there is a deterioration of the vascular hemodynamic component in normal murine ageing[40] and an increase in blood flow associated with anxiousness in TrJ mice in comparison to WT mice[41].

Methods

Animal preparation

All animal experiments and procedures were approved by the local ethics committee (Comisión de Ética en el Uso de Animales, Instituto de Investigaciones Biológicas Clemente Estable -IIBCE, Uruguay, protocol number: 002a/10/2020). All experiments were carried out in strict accordance with the relevant regulations (Uruguayan law number 18611) and with the ARRIVE guidelines. Wild type *C57BL/6* (WT) and $B6.S2 - Pmp22^{TrJ}$ (TrJ) mice were obtained from Jackson Laboratories. Both colonies were raised at the IIBCE animal house in a controlled environment (12 h. dark/12 h. light cycle, average temperature of 21 $\pm 3^{\circ}$C), with unrestricted access to food and water. At 21 days of age the mice were weaned, sexed and numbered by ear punching method, the phenotype of TrJ mice is distinguished from WT by the suspending tail test, as was reported by Rosso et al.[42]. In the experiments only male mice were used.

The first step of the procedure is to anesthetize the mice following a similar procedure as described in Anzibar Fialho et al.[40]. A mixture of ketamine and xylazine, corresponding to the animal's weight, is diluted twofold with saline solution (0.9% NaCl). At first we apply 85% of the dose required for anesthesia, the rest of the dose is administered on demand depending on the inspection of the mouse anesthetic level. To this end, we systematically assessed the anesthetic level by monitoring three physical parameters: (1) slight spontaneous whisker movement; (2) absence of muscular response to pressure on the muscles of a paw; and (3) absence of the corneal reflex. Under these conditions, the mouse remains anesthetized for approximately 40 minutes, enough time to conduct our experiments.

In all experiments, mice were between 2 and 3 months old in order to avoid craniotomy or skull thinning processes. After 10 minutes, when the animal is fully asleep, we apply a depilatory cream to shave the mouse head, and wait for another 10 minutes to remove it and get the skull exposed. After this, the animal is placed on a heating pad (HP-1M, Physitemp, USA) attached to the stereotaxic system. The mouse temperature was held at 37°C using a rectal probe (HP-1M thermocouple, Physitemp, USA) and a heating pad both connected

to a temperature controller (TCAT-2DF, Physitemp, USA). This temperature control is necessary to achieve a sufficient level of reactivity in response to the applied stimulus.

Once the ultrasound probe is aligned to the coronal plane of the brain we move in the anteroposterior axis to place the probe between -1.58mm and -1.82mm from Bregma. This is done by visually matching the structures of the hippocampus and cortex in reference to the Atlas Paxinos & Franklin[43]. This region contains the primary somatosensory cortex barrel field (S1BF) which controls the vibrissae movement.

Functional ultrasound and resting state experiment

The functional ultrasound (fUS) experiment consists of acquiring ultrafast Doppler images while simultaneously applying an ON-OFF pattern of external sensory stimulation to the anesthetized mouse. The stimulation is done by manually moving the vibrissae with a cotton swab. The pattern starts with 60 seconds OFF period, followed by four 40 seconds ON and 40 seconds OFF periods as shown in Fig. 1a, c. The total registration time is 380 seconds at a frame rate of 1 image per second. The systematization of this stimulation protocol is essential to obtain consistent and reliable data. To avoid any confounding factors, whisker stimulation was performed consistently by the same researcher. Before the fUS experiment, we perform a resting state (RS) experiment acquiring 380 seconds of coronal images without applying any external stimuli. Between the RS and the fUS experiment, we do a visual inspection of the mouse and apply the remaining dose of anesthesia if needed.

Acquisition of ultrafast Doppler images was done using a 128 elements, 15 MHz probe (Vermon) driven by a Verasonics Vantage system following a similar procedure as in Anzibar Fialho et al.[40]. Each ultrafast Doppler image was obtained by averaging 350 compound images. Each compound image is formed by adding coherently plane-wave emissions from four angles (-6,-2,2,6). For each angle, we perform three plane wave emissions and average the backscattered echoes in order to increase the signal to noise ratio. The Doppler frame rate was set to

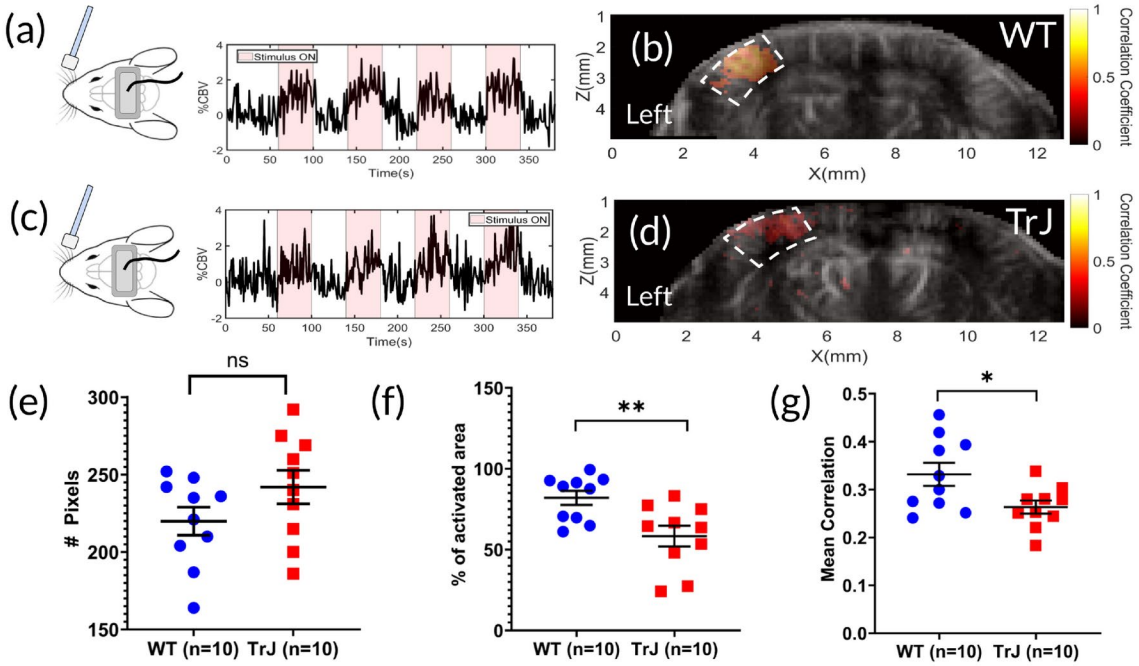

Fig. 1. Left primary somatosensory cortex barrel field (S1BF L) activation by vibrissae stimulation. (**a**) representative WT and (**c**) representative TrJ mouse images (taken from https://zenodo.org/record/3925903). The mice were stimulated manually by moving periodically the right vibrissae (contralateral side of activation) whilst acquiring the functional Ultrasound (fUS) images. In both cases, the measured variation of cerebral blood volume relative to the first 20 seconds (% CBV) for a representative pixel in the S1BF L region are shown as a solid black line, with the stimulation windows represented as shaded areas. (**b**) and (**d**) activation maps of the vibrissae stimulation for a representative WT and TrJ mouse, respectively. The correlation coefficient between the periodic stimulation pattern and the CBV signal for each pixel are shown in color code (uncoloured pixels have non-significant correlation values: $p > 0.01$), in both cases. WT (**b**) and TrJ (**d**) S1BF L region are highlighted by white dashed lines. (**e**) Number of pixels in the S1BF L region (i.e., region's size) for each mouse according to genotype: WT (n=10) and TrJ (n=10) mice. The Shapiro–Wilk normality test gives $p = 0.394$ and $p = 0.932$ for WT and TrJ, respectively. No significant (ns) differences between genotypes were found using Student's t-test ($p = 0.135$). (**f**) Percentage of activated pixels (coloured pixels in panel (**b**) and (**d**)) with respect to the S1BF L size for each mouse according to genotype. The Shapiro–Wilk normality test gives $p = 0.115$ and $p = 0.311$ for WT and TrJ, respectively. Significant differences between genotypes were found using Student's t-test ($p = 0.007$). (**g**) Mean correlation value of activated pixels in the S1BF L region for each mouse according to genotype. The Shapiro–Wilk normality test gives $p = 0.387$ and $p = 0.977$ for WT and TrJ, respectively. Significant differences between genotypes appear using Student's t-test ($p = 0.024$).

500Hz. The pixel resolution in the axial and lateral pitch is 0.1mm, and we took images of 41 pixels in depth and 128 pixels in width. After compounding, the final image frame rate for one ultrafast Doppler image was 1 second. This corresponds to the fUS time resolution.

As a clutter filter we use a singular value decomposition with denoising[44]. The first singular values of the ultrasound signal are associated with tissue movement (i.e. to high energy and highly correlated spatiotemporal signals), while the last singular values are associated with noise (poor spatiotemporal correlation and low energy signals). To this end we must choose the cut-off values N_{tissue} and N_{noise} that optimize the filter to get blood movement. Using an optimization approach as described in Anzibar Fialho et al.[40], we use $N_{tissue} = 35$ and $N_{noise} = 200$.

Image processing

After acquisition and clutter filtering, we have two matrix datasets for each mouse, where each set contains 380 images of 128×41 pixels. These datasets correspond to the RS and stimulation (fUS) experiment correspondingly, which we preprocess as follows. Firstly, we remove signals coming from outside the skull by manually drawing over each image a binary mask that keeps signals from inside the skull and discards those from outside. Secondly, we divide the skull-free image into anatomical regions by performing a brain atlas coregistration. Specifically, we overlap the Doppler images with coronal planes of the Atlas Paxinos and Franklin, using the planes 44, 45 and 46. To match the brain structure from the Doppler image to the Atlas parcellation, we apply free scale and rotation transformations to the Atlas image. Then, we manually draw over the Doppler image the 8 coregistered anatomical regions, as it is shown in Fig. 3a. These regions are symmetrical for both hemispheres and correspond to the primary somatosensory cortex barrel field (S1BF), association cortex / retrosplenial dysgranular cortex (AC/RSD), retrosplenial granular cortex (RSG), and hippocampus (Hip).

The first step to analyze the CBV signal on any pixel of the image is to convert it to a comparable magnitude between mice. To this end, we compute the relative change in CBV,

$$\%CBV(t) = 100 \times (\frac{CBV(t) - CBV_B}{CBV_B}) \tag{1}$$

where $CBV(t)$ corresponds to the Doppler signal measured at a given pixel and CBV_B is its mean value over the first 20 s when there is no stimulus.

Activation maps

Activation maps represent the activated parts of the brain when a specific stimulation is applied. We construct activation maps for a periodic sensory stimulation of the mice's vibrissae by correlating each pixel's CBV signal from the fUS measurement with the stimulation signal. Moreover, we remove from the activation map those correlation values that are not significant by setting a p-value threshold of 0.01 (namely, we discard correlations that could be attributed to randomness). This results in a mouse-dependent activation map with values between 1 and -1 for each pixel, where 1 is a perfect correlation to the stimulation signal and -1 is a perfect anticorrelation. Activation maps are then displayed as a color map, on top of the Doppler image in grayscale (Fig. 1b,d for WT and TrJ respectively). We set the color scale between 0 and 1 to enhance visualization, since no negative correlation values were obtained.

S1BF analysis

To characterize the activation of the S1BF region of each mouse (Fig. 1b,d), we first compute the percentage of activated area, defined as the ratio of pixels with significant correlation inside S1BF compared with the total amount of pixels in S1BF. We consider significant correlation to those pixels whose time signal correlate with stimulus with a $p < 0.01$. For each mouse, we also compute the mean correlation value of the activated pixels inside S1BF.

Secondly, we compute the response rate for each mouse. This was done by considering the time signal of the pixels in the activated area (those significantly correlated with stimulus), low-pass filtered with a cut-off frequency 0.01Hz - as seen in Fig. 2a. For each filtered signal, we consider 6 time points (corresponding to 6 seconds) after the beginning of each stimulus to compute the slope of the curve in $\%CBV/sec$ (yellow line in Fig. 2a). Therefore, for each pixel we have four slope values corresponding to the four stimulation stages of the periodic stimulation pattern. Then, for each mouse we compute the mean slope value for each stimulus by averaging the slope of all the activated pixels in the S1BF region. Thus, for each genotype and each stimulus we have a list of slope values corresponding to all the mice in the group.

Finally, we evaluate the amplitude of the signal in the moments when the stimulus is ON against those when the stimulus is OFF. This gives us a measure of the difference in blood perfusion between activation and basal state. For this, we consider again the activated pixels in S1BF, and compute the mean $\%CBV$ value during stimulation, which we call $\%CBV_{ON}$ (violet in Fig. 2d), and we calculate a $\%CBV_{OFF}$ value for each stimulus as the mean $\%CBV$ value in the 40 s prior to each stimulation begins (orange in Fig. 2d). Then, for each stimulus we analyze the difference between the ON value and OFF value, that is $< \%CBV_{ON} > - < \%CBV_{OFF} >$.

Brain functional connectivity

To study brain connectivity, we section the Doppler image in the anatomic regions shown in Fig. 3a, and compute a representative time signal for each region by averaging the time signals $CBV(t)$ over the corresponding region. Therefore, for each mouse we have 8 region-averaged signals for the stimulation and RS experiments. For each experiment, we pairwise correlate these signals (8x7/2 = 28 pairs). This results in a correlation matrix M, where

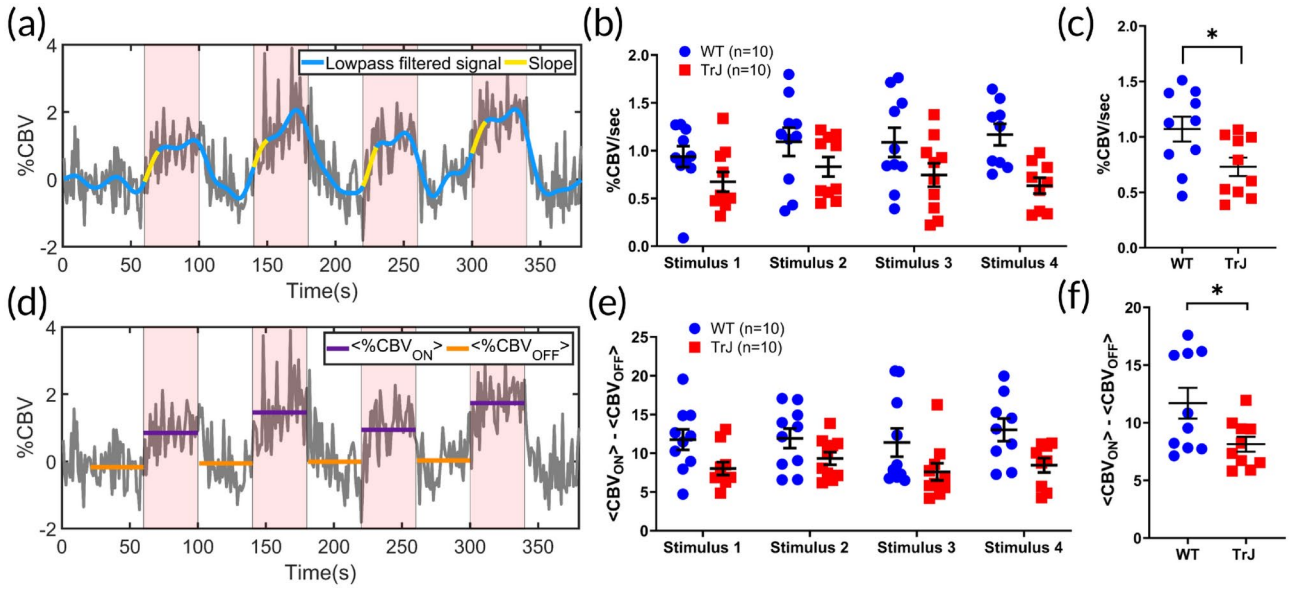

Fig. 2. Hemodynamic response in the S1BF L region to vibrissae stimulation. (**a**) Example of a mouse's variation in blood perfusion ($\%CBV$) for one representative pixel in the S1BF L region as a function of time (grey continuous line). The %CBV rate, corresponds to the slope (yellow line segments) computed from the response to each vibrissae stimulation, (shaded pink areas) obtained from the 6 seconds immediately after the stimulation starts in the low-pass filtered $\%CBV$ signal (blue solid line), with a cut-off frequency of 0.01Hz. (**b**) For each stimulus (4 slopes), we register the pixel-averaged slope per mouse and genotype from all the activated pixels in the S1BF L region ($\%CBV/sec$) - WT (n=10) and TrJ (n=10) mice. No significant differences emerge between genotypes for each stimulus ($p > 0.05$) using a generalised linear mixed model (GLIMMIX) and post hoc analyses (see Methods for details). (**c**) Mean slope value distribution in WT (blue) and TrJ (red) mice taking into account all the stimuli. Considering only the effect of genotype in the GLIMMIX model we found significant differences (asterisk indicates: $p = 0.024$). (**d**) Example of a mouse's variation in blood perfusion ($\%CBV$) for a representative pixel from the S1BF L region as a function of time (gray continuous line). For each mouse, we register the mean $\%CBV$ signal for each 40-second stimuli (horizontal violet segments), $< \%CBV_{ON} >$, and for the 40 seconds before stimulation (horizontal orange segments), $< \%CBV_{OFF} >$. (**e**) Pixel-averaged $< \%CBV_{ON} > - < \%CBV_{OFF} >$ differences from all the S1BF L activated pixels for each mouse, genotype, and stimulus. No significant differences emerge between genotypes for each stimulus ($p > 0.05$) using a generalised linear mixed model (GLIMMIX) and post hoc analyses (see Methods for details). (**f**) Mean $< \%CBV_{ON} > - < \%CBV_{OFF} >$ differences per mouse and genotype. Considering only the effect of genotype in the GLIMMIX model we found significant differences (asterisk indicates: $p = 0.024$).

the M_{ij} entry is the Pearson's correlation value between the averaged signal of region *i* and the averaged signal of region *j*. Finally, for each genotype and each experiment (stimulation and RS) we obtain a representative correlation matrix by averaging the *M* matrix of each mouse in the group (Fig. 3b,c).

Statistical analysis

For all datasets, we use the Shapiro–Wilk test to verify the normality of the distributions. To study the activation of S1BF we use 10 WT and 10 TrJ mice. For evaluating differences between genotypes of distribution values corresponding to activated areas and correlation values in S1BF (Fig. 1e,f,g), we use an unpaired Student's t-test for normal data and Mann-Whitney test for non normal distributions. To study the global response rate and amplitude of the signal during stimulation (Fig. 2c,f), computed as the mean value of the four stimuli, we perform a Student's t-test for normal data and Mann-Whitney test for non normal distributions for comparing between genotypes. These tests were analyzed using GraphPad Prism 8 software.

To evaluate the S1BF data between genotypes considering the different stimuli (Fig. 2b,e), the mixed procedure GLIMMIX of SAS OnDemand for Academics (v. 3.1.0, SAS Institute Inc., Cary, NC, USA) was performed. Fixed effects of genotype, stimuli, and their interactions were included in the model. The animal within each genotype was considered as a random effect. Post hoc analyses were performed by the least square difference (LSD) adjusted by Tukey.

For studying brain connectivity, we used 8 WT and 8 TrJ mice for both the fUS and RS experiments, with the brain connectivity experiment being conducted on a subset of the mice used in the S1BF activation experiment. Each mouse underwent both the fUS and RS experiments. For each genotype, we compute a representative matrix either for RS or fUS experiment as the mean correlation matrix over the sample. To analyze the connectivity of the brain through the correlations (Fig. 3b,c), a mixed procedure was carried out using the GLIMMIX of SAS OnDemand for Academics (v. 3.1.0, SAS Institute Inc., Cary, NC, USA). Analyses were performed separately,

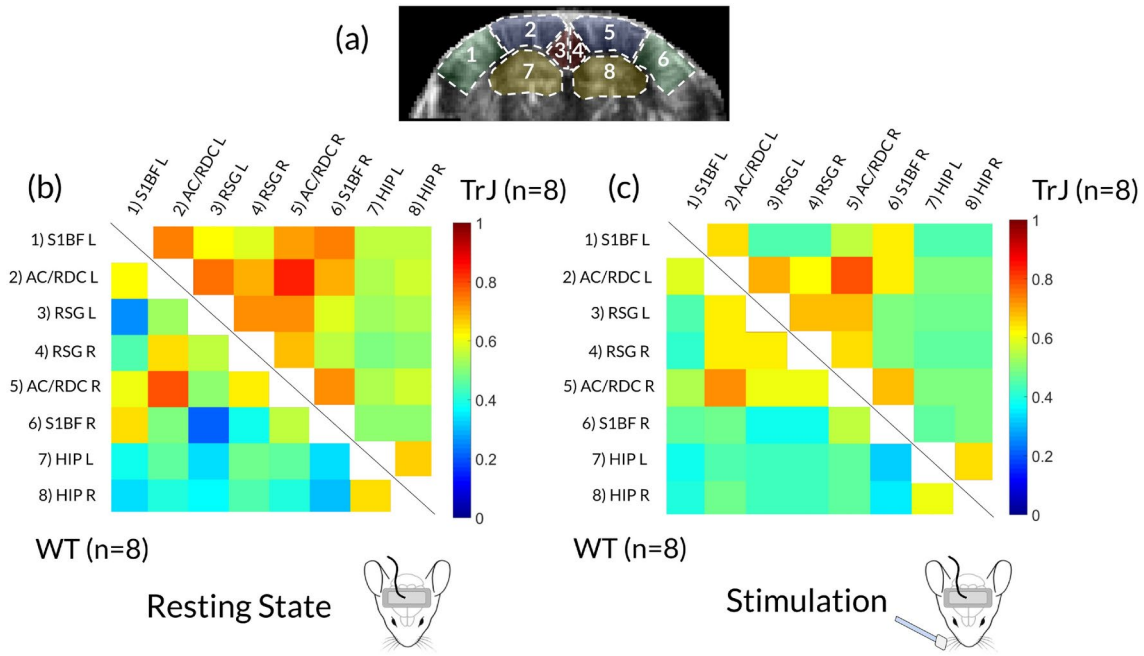

Fig. 3. Brain functional connectivity between brain areas of WT and TrJ during resting state and vibrissae stimulation (fUS experiment). (**a**) Example of a coregistered Doppler image from a mouse's brain and the Paxinos and Franklin atlas (planes 44, 45, and 46), using free scaling and rotation transformations. White dashed lines delimit the 8 (coregistered) anatomical regions, including primary somatosensory cortex barrel field (S1BF: 1 and 6), association cortex/retrosplenial dysgranular cortex (AC/RSD: 2 and 5), retrosplenial granular cortex (RSG: 3 and 4), and hippocampus (HIP: 7 and 8). (**b**) Population-averaged correlation matrix during RS (i.e., without vibrissae stimulation). The upper diagonal entries are the average of (n = 8) TrJ mice and the lower diagonal entries are the average of (n = 8) WT mice. (**c**) Population-averaged correlation matrix during stimulation, where entries are analogous as in panel (**b**).

either for RS (Fig. 3b) or for stimulation (Fig. 3c). Within each of the respective analysis (RS or stimulation), the model included the fixed effects of genotype, brain region, and the respective interaction. The animal within each genotype was considered as a random effect. Post hoc analyses were performed by the least square difference (LSD) adjusted by Tukey.

All results are expressed as the mean ± standard error of the mean (SEM). Significance was considered with an $\alpha \leq 0.05$, and trend for values between 0.05 and 0.10.

Results

Activation of S1BF region in response to vibrissae stimulation

All the mice considered in this study have a similar response to right wisker stimulus as the one shown in Fig. 1b,d, corresponding to a localized activation of the S1BF Left region (S1BF L) for WT and TrJ models, respectively. The total amount of pixels in the S1BF L region was comparable between TrJ and WT genotypes (Fig. 1e shows no significant differences, $p = 0.135$), which indicates, as expected, that the anatomical regions remain similar between groups, so no bias is added to later results. On the other hand, the percentage of pixels activated in the S1BF L region shows significant differences between genotypes (Fig. 1f, $p = 0.007$), and as can be seen the WT genotype has greater activation area than TrJ. These two results confirm that changes in activation area are due to physiological factors and not by the methodology of region delimitation. Also, on Fig. 1g we present the results for the mean correlation value of the activated pixels in the S1BF L region. As can be seen, we found significant differences between genotypes ($p = 0.024$), as the mean correlation value for WT is higher than in TrJ mice. This suggests that, not only the activation area is affected in TrJ, but also the strength of the activation is compromised. In brief, the activation in TrJ mice is diminished when compared to WT mice.

To analyze the response rate, we measured the slope of the signal during each stimulation period (Fig. 2a, yellow lines). Figure 2b depicts the slope distribution, measured as the relative variation of blood perfusion per second ($\%CBV/sec$) for each stimulus. Considering the effects of genotype, stimulus, and interaction between them, the model gives significant differences only for genotype's comparison (Fig. 2c, $p = 0.024$). The global slope in each genotype –computed as the mean slope for all stimuli– was significantly higher in WT (1.074 ± 0.099 $\%CBV/sec$) than in TrJ ($0,727 \pm 0.099$ $\%CBV/sec$). No differences were found for effect of stimulus ($p = 0.196$) nor for the effect of interaction between stimulus and genotype ($p = 0.298$).

In Fig. 2e we show the difference between $\%CBV_{ON}$ and $\%CBV_{OFF}$ discriminated by stimulus. Again, considering the effects of genotype, stimulus, and interaction between them, the model gives significant differences only for genotype's comparison (Fig. 2f, p = 0.024). Considering genotype, the mean value is greater

in WT (11.99 ± 1.03) than in TrJ (8.41 ± 1.03). No differences were found for the effect of stimulus ($p = 0.296$) nor for the effect of interaction between stimulus and genotype ($p = 0.753$).

Brain connectivity during resting state and during vibrissae stimulation

Figure 3a shows the brain areas considered for the resting state (RS) and stimulation (fUS experiment) connectivity analysis in both genotypes. The comparisons between genotype areas during RS and fUS experiments are shown in the correlation matrices of Fig. 3b,c, respectively. In both figures, the color-coded entries below the diagonal of the correlation matrix represent the population-average for WT, and those above the diagonal represent the population-average for TrJ. In the supplementary information we show the explicit values for each entry of these matrices and *p*-values for comparison (see Supplementary Figs. S1 and S2).

In RS experiments, the global connectivity –evaluated by the mean correlation value between the spontaneously activated areas– was significantly greater in TrJ than in WT (TrJ: 0.624 ± 0.038 vs. WT: 0.472 ± 0.038; $p = 0.015$ considering fix effect of genotype in GLIMMIX model). We also find a significant interaction between genotype and matrix entry ($p < 0.0001$). This indicates that for the same matrix entry there is a different behaviour when comparing between both genotypes. In particular, one of the main differences can be seen in the connectivity between S1BF regions and hippocampus. For example, if we consider S1BF L connectivity with both hippocampus regions, we see that in TrJ it is significantly greater than in WT ($p = 0.047$ and $p = 0.007$ for left and right hippocampus respectively).

During stimulation, the global connectivity –evaluated by the mean correlation value between stimulus activated areas– was similar between both genotypes (WT: 0.488 ± 0.041, and TrJ: 0.552 ± 0.041; $p = 0.287$ considering fix effect of genotype in GLIMMIX model). There was no significant interaction between genotype and matrix entry ($p = 0.402$). In this case, the main differences can be seen between S1BF R and S1BF L ($p = 0.021$).

Considering the connectivity going from RS to stimulation, we detect differences between both genotypes. The connectivity of S1BF L region with S1BF R decreased 28% in WT and 14% in TrJ. The connectivity between S1BF L-RSG L increased 73% for WT, but for TrJ we observed a decrease of 27%. The same antagonic genotype behaviour can be observed for the connectivity of S1BF R region with RSG L and RSG R. Similarly, we compare the connectivity between S1BF L-HIP L and S1BF L-HIP R, where we observed only an increase of 20% in WT for S1BF L-HIP R, but a decrease of 19% for TrJ for both regions (S1BF L-HIP L and S1BF L-HIP R). In addition, for S1BF R-HIP R there is an increase in WT (16%) and a decrease in TrJ (6%). The change in connectivity for other regions can be seen in the supplementary information (Fig. S3).

Discussion

The present work demonstrates the existence of hemodynamic differences at the cerebral level between TrJ and WT mice. The differences are expressed both in response to the external stimulus of vibrissae and in resting state conditions. These findings suggest structural and/or functional changes in the cerebral cortex associated to both genotypes: healthy or neuropathologic.

Resting state functional brain networks have been widely studied in rodents, and the major networks have been established using functional MRI[45]. It has been reported in rats that the ability to discriminate bilateral tactile information from unilateral stimulation of the vibrissae is related to interhemispheric connectivity between both regions of the somatosensory cortex (S1BF)[46–48]. Shuler et al.[46,47] demonstrated that the direct activation of unilateral S1BF mouse region resulted in hypoperfusion of the contralateral barrel cortex, even when subcortical processes were skipped. This asymmetric perfusion could relate to a loss in functional connectivity between these two regions.

Ferrier and coworkers[34] studied brain connectivity in WT mice during vibrissae path stimulation. They observed that during stimulation-on, S1BF L and S1BFR showed lower connectivity values than in stimulus-off. We observed, for WT, a similar interhemispheric disconnection performance between the S1BF regions when comparing stimulation and RS (Fig. 3). Also, high interhemispheric connectivity between hippocampus is expected in resting state for WT mice[45], since CBV signals are strongly related in this structure[49]. In Ferrier et al.[34] they report higher connectivity in the hippocampus region during stimulation as compared to basal state. In our case, we report similar high connectivity values during resting state and stimulation for WT mice. However, our resting state experiment differs from what Ferrier et al. report as baseline, since we do resting state experiment of 380 seconds with no external stimulation applied to the brain, and they compute a resting state baseline by concatenating OFF periods duringperiodic stimulation experiments. We consider that our methodology is more adequate to compare the brain in two different states, one with a specific task and another with no specific task. More importantly our experiment represents a true resting state analysis and can be compared with previous work related to resting state functional brain networks[50].

It is also important to consider that the fUS recording of the somatosensory response to the vibrissae motor stimulus is not exclusively central, but involves a partially peripheral response, integrated by the trigeminal pathway. This fact could, at least partially, justify the hemodynamic decrease observed in the S1BF L TrJ response to the motor stimulus (lesser number of activated pixels with lesser strength, and lower slope and amplitude of CBV signal response) compared to WT, since cranial pair V is also myelinated by Schwann cells, which are particularly affected in this CMT1E model by the *pmp22* mutation.

In this sense, Shatz and Stryker[51] and Hubel et al.[52] reported that the spontaneous activity of neurons is critical for the formation of precise and orderly neuronal connections in the central nervous system. This fact indicates the need for typical stimuli for normal brain development. Also, it has been reported that the cortex, particularly the somatosensory cortex, can undergo structural and functional reorganization in response to peripheral nerve alterations when incoming peripheral sensory activity is interrupted or modified (reversibly or irreversibly)[53]. Moreover, in monkeys with lesions in peripheral nerves, expansion of innervated cortical areas

towards non-innervated areas (adjacent or remote) and discontinuous patches of sensory representation were observed[54]. In human peripheral neuropathies, structural and functional rearrangement in the somatosensory cortex has been reported using MRI. Alterations were detected in the diabetic peripheral neuropathy[55], and interestingly, in key brain areas of CMT patients[56]. It was suggested that the brain structural reorganization could be an adaptive response to axonal degeneration caused by the CMT disease, and that structural changes can extend beyond the somatosensory cortex, affecting whole brain connectivity[57]. Besides, differences in the human cortical activation were also observed while applying a sensory stimulus to the limbs[58].

This background allows us to suggest that the demyelination of the peripheral sector of the trigeminal nerve due to the *pmp22* mutation in TrJ mice could affect nerve conduction to the somatosensory cortex, generating structural and/or functional modifications and connectivity alterations in both stimulation and RS.

Functional brain connectivity has proven to be a suitable tool to study the effects of many major neurodegenerative diseases to the central nervous system. For example, it has been shown that patients with Alzheimer disease (AD) present alterations of several functional brain networks[59,60]. Specifically, in Agosta et al.[61] they show a rewiring of the sensorimotor network in patients with AD, which occupies a main role in our work as is the region activated by stimulus.

More importantly, some research elucidates changes in human brain functional connectivity for CMT disease from fMRI. In the work of Pontillo et al.[62], they found increased resting state FC in patients with CMT compared to healthy controls, in several of the well known brain regions corresponding to the default mode network (DMN) (visual, salience, dorsal, language). In our work, we found an increase in global connectivity during resting state for TrJ when compared to WT. In particular, in Ferrier et al.[34], RSG is defined as a possible DMN hub in mice brain. In our case, these regions appear more connected in TrJ than in WT. In the work of Pontillo et al.[62], they show that task-positive regions have increased connectivity with task-negative regions involved in DMN in patients with CMT, which is contrary to healthy expected behaviour. In our work this is also observed if we considered the stronger connections between S1BF (task-positive regions) and RSG (DMN hub) in TrJ as opposed to weaker connections observed in WT (Fig. 3). The correct functional relationship between task-positive and task-negative areas is strongly associated with cognitive process[63] and goal-directed behaviour[64]. Our findings regarding task-positive and task-negative relationships could be related to previous studies where TrJ mice present anxious behaviour associated with hippocampal domains[19]. As observed in some human neurodegenerative diseases[65], it could be speculated that the increased functional connectivity observed in TrJ could be related to cognitive impairment, but this requires further investigation.

Under RS, TrJ mice show different global brain connectivity as well as between the different regions of the same coronal section. The increased connectivity in RS of TrJ compared to WT suggests a significant alteration in the modulation of TrJ cerebral blood flow. This may be due to a failure of the global connectivity maintenance mechanisms as a result of an altered vascular physiology, with perhaps a preponderance of spontaneous global vasomotion (Mayer waves) over local neurovascular coupling. We have recently demonstrated that in RS, the CBV of TrJ mice, showed a significantly increased value with respect to WT mice, associated with significant vessel volume values increase, detectable as early as three months old mice[41].

This TrJ hemodynamics was related to a specific hippocampal-based anxious behaviour. It is interesting to note that the hippocampus was highly connected to the cortical somatosensory areas in this genotype, a behaviour that could help to understand the existence of the higher basal connectivity observed in RS.

Understanding the mechanisms underlying cortical plasticity in peripheral neuropathies could pave the way for potential interventions aimed at promoting functional recovery in affected individuals. Further exploration of this hemodynamic profile will be necessary to gain a deeper understanding of the role of the vascular component in the origin and development of the disease, as well as to assess its response to various stimuli and/or therapeutic approaches.

Conclusions

In summary, the present work demonstrates the existence of hemodynamic differences at the cerebral level between TrJ and WT mice. We found alterations in the activation of the sensorimotor cortex region and functional connectivity (FC). Specifically, TrJ mice present a diminished response regarding activation area, %CBV rate of change and %CBV amplitude during stimulation. Concerning FC, TrJ presents higher global connectivity in resting state than WT, and loss of interhemispheric correspondence of sensorimotor cortex while receiving sensory stimulation. Our results indicate that there is an identifiable genotype-specific RS/stimulation hemodynamic brain profile associated with a normal and with neuropathologic condition. These findings in the TrJ model suggest a central nervous system compromise that could shift our understanding of the CMT1E disease.

Data availibility

Data is available upon reasonable request to the corresponding authors.

Received: 8 July 2024; Accepted: 14 November 2024
Published online: 03 December 2024

References

1. Pisciotta, C. & Shy, M. E. *Hereditary neuropathy.* **195**, 609–617 (2023).
2. Morena, J., Gupta, A. & Hoyle, J. C. Charcot-Marie-Tooth: From molecules to therapy. *Int. J. Mol. Sci.* **20**, 3419 (2019).
3. Bird, T.D. Charcot-Marie-Tooth hereditary neuropathy overview. *GeneReviews* (1993).
4. Murakami, T. & Sunada, Y. Schwann cell and the pathogenesis of Charcot–Marie–Tooth disease. *Myelin Basic Clin. Adv.* 301–321 (2019).

5. Li, J., Parker, B., Martyn, C., Natarajan, C. & Guo, J. The pmp22 gene and its related diseases. *Mol. Neurobiol.* **47**, 673–698 (2013).
6. Jaradeh, S. S. Hereditary neuropathies. *J. Clin. Neuromuscul. Dis.* **5**, 72–80 (2003).
7. Tobler, A. R., Liu, N., Mueller, L. & Shooter, E. M. Differential aggregation of the trembler and trembler J mutants of peripheral myelin protein 22. *J. Peripher. Nerv. Syst.* **7**, 206–207 (2002).
8. Myers, J. K., Mobley, C. K. & Sanders, C. R. The peripheral neuropathy-linked trembler and Trembler-J mutant forms of peripheral myelin protein 22 are folding-destabilized. *Biochemistry* **47**, 10620–10629 (2008).
9. Valentijn, L. J. et al. Identical point mutations of PMP-22 in Trembler-J mouse and Charcot-Marie-Tooth disease type 1a. *Nat. Genet.* **2**, 288–291 (1992).
10. Opalach, K., Rangaraju, S., Madorsky, I., Leeuwenburgh, C. & Notterpek, L. Lifelong calorie restriction alleviates age-related oxidative damage in peripheral nerves. *Rejuvenation Res.* **13**, 65–74 (2010).
11. Rangaraju, S. et al. Molecular architecture of myelinated peripheral nerves is supported by calorie restriction with aging. *Aging Cell* **8**, 178–191 (2009).
12. Russo, M. et al. Variable phenotypes are associated with pmp22 missense mutations. *Neuromuscul. Disord.* **21**, 106–114 (2011).
13. Notterpek, L., Fortun, J. & Ferguson, T. Aggregation of peripheral myelin protein 22 in trembler j neuropathy nerves. *J. Neurochem.* **81**, 77–77 (2002).
14. Quarles, R. Myelin sheaths: Glycoproteins involved in their formation, maintenance and degeneration. *Cell. Mol. Life Sci. CMLS* **59**, 1851–1871 (2002).
15. Notterpek, L. & Tolwani, R. J. Experimental models of peripheral neuropathies. *Comp. Med.* **49**, 588–599 (1999).
16. Chin, L., Olzmann, J. & Li, L. Aggresome formation and neurodegenerative diseases: Therapeutic implications. *Curr. Med. Chem.* **15**, 47–60 (2008).
17. Sinclair, D. A. Toward a unified theory of caloric restriction and longevity regulation. *Mech. Ageing Dev.* **126**, 987–1002 (2005).
18. Di Tomaso, M. V. et al. Colocalization analysis of peripheral myelin protein-22 and Lamin-B1 in the Schwann Cell Nuclei of Wt and TrJ Mice. *Biomolecules* **12**, 456 (2022).
19. Damián, J. P. et al. Central alteration in peripheral neuropathy of Trembler-J mice: Hippocampal pmp22 expression and behavioral profile in anxiety tests. *Biomolecules* **11**, 601 (2021).
20. Deffieux, T., Demené, C. & Tanter, M. Functional ultrasound imaging: A new imaging modality for neuroscience. *Neuroscience* **474**, 110–121 (2021).
21. Macé, E. et al. Functional ultrasound imaging of the brain. *Nat. Methods* **8**, 662–664 (2011).
22. Gesnik, M. et al. 3d functional ultrasound imaging of the cerebral visual system in rodents. *Neuroimage* **149**, 267–274 (2017).
23. Blaize, K. et al. Functional ultrasound imaging of deep visual cortex in awake nonhuman primates. *Proc. Natl. Acad. Sci.* **117**, 14453–14463 (2020).
24. Dizeux, A. et al. Functional ultrasound imaging of the brain reveals propagation of task-related brain activity in behaving primates. *Nat. Commun.* **10**, 1400 (2019).
25. Imbault, M., Chauvet, D., Gennisson, J.-L., Capelle, L. & Tanter, M. Intraoperative functional ultrasound imaging of human brain activity. *Sci. Rep.* **7**, 7304 (2017).
26. Demene, C. et al. Functional ultrasound imaging of brain activity in human newborns. *Sci. Transl. Med.* **9**, eaah6756 (2017).
27. Baranger, J. et al. Bedside functional monitoring of the dynamic brain connectivity in human neonates. *Nat. Commun.* **12**, 1080 (2021).
28. Schaeffer, S. & Iadecola, C. Revisiting the neurovascular unit. *Nat. Neurosci.* **24**, 1198–1209 (2021).
29. Sieu, L.-A. et al. EEG and functional ultrasound imaging in mobile rats. *Nat. Methods* **12**, 831–834 (2015).
30. Bourgeais-Rambur, L. et al. Altered cortical trigeminal fields excitability by spreading depolarization revealed with in vivo functional ultrasound imaging combined with electrophysiology. *J. Neurosci.* **42**, 6295–6308 (2022).
31. Nunez-Elizalde, A. O. et al. Neural correlates of blood flow measured by ultrasound. *Neuron* **110**, 1631–1640 (2022).
32. Aydin, A.-K. et al. Transfer functions linking neural calcium to single voxel functional ultrasound signal. *Nat. Commun.* **11**, 2954 (2020).
33. Osmanski, B.-F., Pezet, S., Ricobaraza, A., Lenkei, Z. & Tanter, M. Functional ultrasound imaging of intrinsic connectivity in the living rat brain with high spatiotemporal resolution. *Nat. Commun.* **5**, 5023 (2014).
34. Ferrier, J., Tiran, E., Deffieux, T., Tanter, M. & Lenkei, Z. Functional imaging evidence for task-induced deactivation and disconnection of a major default mode network hub in the mouse brain. *Proc. Natl. Acad. Sci.* **117**, 15270–15280 (2020).
35. Hikishima, K. et al. Brain-wide mapping of resting-state networks in mice using high-frame rate functional ultrasound. *Neuroimage* **279**, 120297 (2023).
36. de Paz, J. M. M. & Macé, E. Functional ultrasound imaging: A useful tool for functional connectomics?. *Neuroimage* **245**, 118722 (2021).
37. Rahal, L. et al. Ultrafast ultrasound imaging pattern analysis reveals distinctive dynamic brain states and potent sub-network alterations in arthritic animals. *Sci. Rep.* **10**, 10485 (2020).
38. Rabut, C. et al. Pharmaco-fUS: Quantification of pharmacologically-induced dynamic changes in brain perfusion and connectivity by functional ultrasound imaging in awake mice. *Neuroimage* **222**, 117231 (2020).
39. Vidal, B. et al. Functional ultrasound imaging to study brain dynamics: Application of pharmaco-fUS to atomoxetine. *Neuropharmacology* **179**, 108273 (2020).
40. Anzibar Fialho, M. et al. Intensity distribution segmentation in ultrafast doppler combined with scanning laser confocal microscopy for assessing vascular changes associated with ageing in murine hippocampi. *Sci. Rep.* **12**, 6784 (2022).
41. Martínez Barreiro, M. et al. In vivo ultrafast doppler imaging combined with confocal microscopy and behavioral approaches to gain insight into the central expression of peripheral neuropathy in Trembler-J mice. *Biology* **12**, 1324 (2023).
42. Rosso, G. et al. Early phenotypical diagnoses in Trembler-J mice model. *J. Neurosci. Methods* **190**, 14–19 (2010).
43. Paxinos, G. & Franklin, K. B. *Paxinos and Franklin's the Mouse Brain in Stereotaxic Coordinates* (Academic press, Cambridge, 2019).
44. Baranger, J. et al. Adaptive spatiotemporal SVD clutter filtering for ultrafast doppler imaging using similarity of spatial singular vectors. *IEEE Trans. Med. Imaging* **37**, 1574–1586 (2018).
45. Nasrallah, F. A., Tay, H.-C. & Chuang, K.-H. Detection of functional connectivity in the resting mouse brain. *Neuroimage* **86**, 417–424 (2014).
46. Shuler, M. G., Krupa, D. J. & Nicolelis, M. A. Integration of bilateral whisker stimuli in rats: Role of the whisker barrel cortices. *Cereb. Cortex* **12**, 86–97 (2002).
47. Shuler, M. G., Krupa, D. J. & Nicolelis, M. A. Bilateral integration of whisker information in the primary somatosensory cortex of rats. *J. Neurosci.* **21**, 5251–5261 (2001).
48. Böhm, M. et al. Neurovascular coupling during optogenetic functional activation: Local and remote stimulus-response characteristics, and uncoupling by spreading depression. *J. Cerebral Blood Flow Metab.* **40**, 808–822 (2020).
49. Sforazzini, F., Schwarz, A. J., Galbusera, A., Bifone, A. & Gozzi, A. Distributed bold and CBV-weighted resting-state networks in the mouse brain. *Neuroimage* **87**, 403–415 (2014).
50. Zerbi, V., Grandjean, J., Rudin, M. & Wenderoth, N. Mapping the mouse brain with rs-fMRI: An optimized pipeline for functional network identification. *Neuroimage* **123**, 11–21 (2015).
51. Shatz, C. J. & Stryker, M. P. Ocular dominance in layer IV of the cat's visual cortex and the effects of monocular deprivation. *J. Physiol.* **281**, 267–283 (1978).

52. Hubel, D. H., Wiesel, T. N., LeVay, S., Barlow, H. B. & Gaze, R. M. Plasticity of ocular dominance columns in monkey striate cortex. *Philos. Trans. R. Soc. Lond. B Biol. Sci.* **278**, 377–409 (1977).
53. Makin, T. R. et al. Phantom pain is associated with preserved structure and function in the former hand area. *Nat. Commun.* **4**, 1570 (2013).
54. Garraghty, P. E. & Kaas, J. H. Large-scale functional reorganization in adult monkey cortex after peripheral nerve injury. *Proc. Natl. Acad. Sci.* **88**, 6976–6980 (1991).
55. Selvarajah, D. et al. Structural and functional abnormalities of the primary somatosensory cortex in diabetic peripheral neuropathy: A multimodal MRI study. *Diabetes* **68**, 796–806 (2019).
56. Pontillo, G. et al. Brain plasticity in Charcot-Marie-Tooth type 1a patients? A combined structural and diffusion MRI study. *Front. Neurol.* **11**, 795 (2020).
57. Rocca, M. A. et al. Brain connectivity abnormalities extend beyond the sensorimotor network in peripheral neuropathy. *Hum. Brain Mapp.* **35**, 513–526 (2014).
58. Wang, Z. et al. Cortical activation reorganization of cerebral regions in Charcot-Marie-Tooth patients: A task-state functional magnetic resonance imaging study. *J. Orthop. Sports Med.* **4**, 276–288 (2022).
59. Brier, M. R. et al. Loss of intranetwork and internetwork resting state functional connections with Alzheimer's disease progression. *J. Neurosci.* **32**, 8890–8899 (2012).
60. Sheline, Y. I. & Raichle, M. E. Resting state functional connectivity in preclinical Alzheimer's disease. *Biol. Psychiat.* **74**, 340–347 (2013).
61. Agosta, F. et al. Sensorimotor network rewiring in mild cognitive impairment and Alzheimer's disease. *Hum. Brain Mapp.* **31**, 515–525 (2010).
62. Pontillo, G. et al. Diffuse brain connectivity changes in Charcot-Marie-Tooth type 1a patients: A resting-state functional magnetic resonance imaging study. *Eur. J. Neurol.* **28**, 305–313 (2021).
63. Hampson, M., Driesen, N., Roth, J. K., Gore, J. C. & Constable, R. T. Functional connectivity between task-positive and task-negative brain areas and its relation to working memory performance. *Magn. Reson. Imaging* **28**, 1051–1057 (2010).
64. Kelly, A. C., Uddin, L. Q., Biswal, B. B., Castellanos, F. X. & Milham, M. P. Competition between functional brain networks mediates behavioral variability. *Neuroimage* **39**, 527–537 (2008).
65. Hawellek, D. J., Hipp, J. F., Lewis, C. M., Corbetta, M. & Engel, A. K. Increased functional connectivity indicates the severity of cognitive impairment in multiple sclerosis. *Proc. Natl. Acad. Sci.* **108**, 19066–19071 (2011).

Acknowledgements

This work was mainly funded by the Agencia Nacional de Investigación e Innovación (ANII), grant FCE_1_2019_1_155539. The authors also thank the support of PEDECIBA-Program for the Development of Basic Sciences, CSIC-UdelaR and the Institut Franco-Uruguayen de Physique (IFUP) funded by PEDECIBA-CNRS-UdelaR. J.P.D., C.N., N.R., A.K. and J.Br. thank SNI-ANII. M.A.F., M.M. and L.V.A. thank the support of ANII through scholarships POS_NAC_M_2020_1_164127, POS_FCE_2020_1_1009181 and POS_NAC_2022_1_173578, respectively. N.R. thanks the support of CSIC I+D group grant CSIC2018-FID 13-Grupo ID 722. C.N., A.K. and J.Br. thank grant CSIC-Grupos I+D 497725-2023-2027.

Author contributions

C.N., N.R., A.K. and J.Br. conceived the study. C.N., N.R., A.K. and J.Br. designed and supervised the study. J.Ba. and J.Br. programmed the ultrasound sequence and ultrasound acquisition software. M.A.F. programmed the signal processing and analysis pipeline. M.A.F. and L.V.A. conducted Doppler image segmentation of anatomical brain regions. M.A.F., M.M., L.V.A., A.K. and J.Br. performed the experiments. J.P.D., M.A.F. and A.K. conducted the statistical analysis. M.A.F., C.N., N.R., A.K. and J.Br. discussed and interpreted results. M.A.F., N.R., A.K. and J.Br. prepared all figures. M.A.F., M.V.D.T., N.R., A.K. and J.Br. wrote the original draft. M.T., C.N., A.K. and J.Br. funding acquisition. C.N., A.K. project administration. All authors edited, reviewed and approved the final manuscript. A.K. and J.Br. contributed equally to this work.

Declarations

Competing interests

M.T. is co-founder and shareholder of Iconeous, a company which commercializes ultrasonic neuroimaging scanners. The remaining authors declare no competing interests.

Additional information

Supplementary Information The online version contains supplementary material available at https://doi.org/10.1038/s41598-024-80022-z.

Correspondence and requests for materials should be addressed to A.K. or J.Br.